Article

Transparent ferroelectric crystals with ultrahigh piezoelectricity

https://doi.org/10.1038/s41586-019-1891-y

Received: 30 May 2019

Accepted: 18 November 2019

Published online: 15 January 2020

Chaorui Qiu[1,9], Bo Wang[2,9], Nan Zhang[1,9], Shujun Zhang[2,3], Jinfeng Liu[1], David Walker[4], Yu Wang[5], Hao Tian[5], Thomas R. Shrout[2], Zhuo Xu[1]*, Long-Qing Chen[2,6,7,8]* & Fei Li[1]*

Transparent piezoelectrics are highly desirable for numerous hybrid ultrasound–optical devices ranging from photoacoustic imaging transducers to transparent actuators for haptic applications[1–7]. However, it is challenging to achieve high piezoelectricity and perfect transparency simultaneously because most high-performance piezoelectrics are ferroelectrics that contain high-density light-scattering domain walls. Here, through a combination of phase-field simulations and experiments, we demonstrate a relatively simple method of using an alternating-current electric field to engineer the domain structures of originally opaque rhombohedral $Pb(Mg_{1/3}Nb_{2/3})O_3$-$PbTiO_3$ (PMN-PT) crystals to simultaneously generate near-perfect transparency, an ultrahigh piezoelectric coefficient d_{33} (greater than 2,100 picocoulombs per newton), an excellent electromechanical coupling factor k_{33} (about 94 per cent) and a large electro-optical coefficient γ_{33} (approximately 220 picometres per volt), which is far beyond the performance of the commonly used transparent ferroelectric crystal $LiNbO_3$. We find that increasing the domain size leads to a higher d_{33} value for the [001]-oriented rhombohedral PMN-PT crystals, challenging the conventional wisdom that decreasing the domain size always results in higher piezoelectricity[8–10]. This work presents a paradigm for achieving high transparency and piezoelectricity by ferroelectric domain engineering, and we expect the transparent ferroelectric crystals reported here to provide a route to a wide range of hybrid device applications, such as medical imaging, self-energy-harvesting touch screens and invisible robotic devices.

Achieving simultaneous high piezoelectricity and perfect transparency in a piezoelectric material has long been a challenge. For example, traditional high-performance piezoelectric transducers are typically made from perovskite ferroelectric ceramics and crystals with chemical compositions that are close to their morphotropic phase boundaries (MPBs), such as $Pb(Zr,Ti)O_3$ (PZT) ceramics and domain-engineered PMN-PT crystals. These materials possess very high d_{33} and k_{33} values[11–14], but they are usually opaque in the visible-light spectrum. On the other hand, the commonly used transparent piezoelectric $LiNbO_3$ crystals and polyvinylidine fluoride (PVDF) polymers[6,7] have good transparency but much lower d_{33} and k_{33} values ($LiNbO_3$: $d_{33} < 40$ pC N^{-1}, $k_{33} \approx 47\%$; PVDF: $d_{33} \approx 20$ pC N^{-1}, $k_{33} \approx 16\%$) that severely limit the acoustic source level, bandwidth and sensitivity of the transducers.

In addition to the extrinsic effects, such as porosity and grain boundaries, which are ubiquitous in ceramics, the poor transparency in PZT ceramics and domain-engineered PMN-PT crystals is closely associated with light scattering and reflection from their ferroelectric domain walls. There are two possible approaches to reducing the light-scattering domain walls. The first is to pole a ferroelectric crystal along the polar direction to achieve a single-domain state. However, the d_{33} value of such single-domain PMN-PT crystals is generally very low[13,14]—much lower than that of [001]-poled multidomain rhombohedral PMN-PT crystals (>1,500 pC N^{-1}). In principle, one could first pole a rhombohedral PMN-PT crystal along the [111] direction to achieve a single-domain state with good transparency, then rotate the crystal to the [001] direction to guarantee high longitudinal piezoelectricity. However, this approach is not feasible in practice (see Methods for a detailed explanation). The second approach is to dramatically reduce the domain sizes by breaking the domains into polar nanoregions with spatial sizes (a few to tens of nanometres) much smaller than the wavelength of visible light, thus greatly improving their light transparency—as observed in La-doped PZT[15,16]. However, improving the transparency using polar nanoregions is achieved at the expense of a markedly reduced remanent polarization and thus very low d_{33} values; therefore, despite more than 50 years of effort, optical functionalities in high-performance piezoelectrics have not been realized.

[1]Electronic Materials Research Laboratory (Key Lab of Education Ministry), State Key Laboratory for Mechanical Behavior of Materials and School of Electronic and Information Engineering, Xi'an Jiaotong University, Xi'an, China. [2]Department of Materials Science and Engineering, The Pennsylvania State University, University Park, PA, USA. [3]ISEM, Australian Institute for Innovative Materials, University of Wollongong, Wollongong, New South Wales, Australia. [4]Department of Physics, University of Warwick, Coventry, UK. [5]School of Physics, Harbin Institute of Technology, Harbin, China. [6]Materials Research Institute, The Pennsylvania State University, University Park, PA, USA. [7]Department of Engineering Science and Mechanics, The Pennsylvania State University, University Park, PA, USA. [8]Department of Mathematics, The Pennsylvania State University, University Park, PA, USA. [9]These authors contributed equally: Chaorui Qiu, Bo Wang, Nan Zhang. *e-mail: xuzhuo@xjtu.edu.cn; lqc3@psu.edu; ful5@xjtu.edu.cn

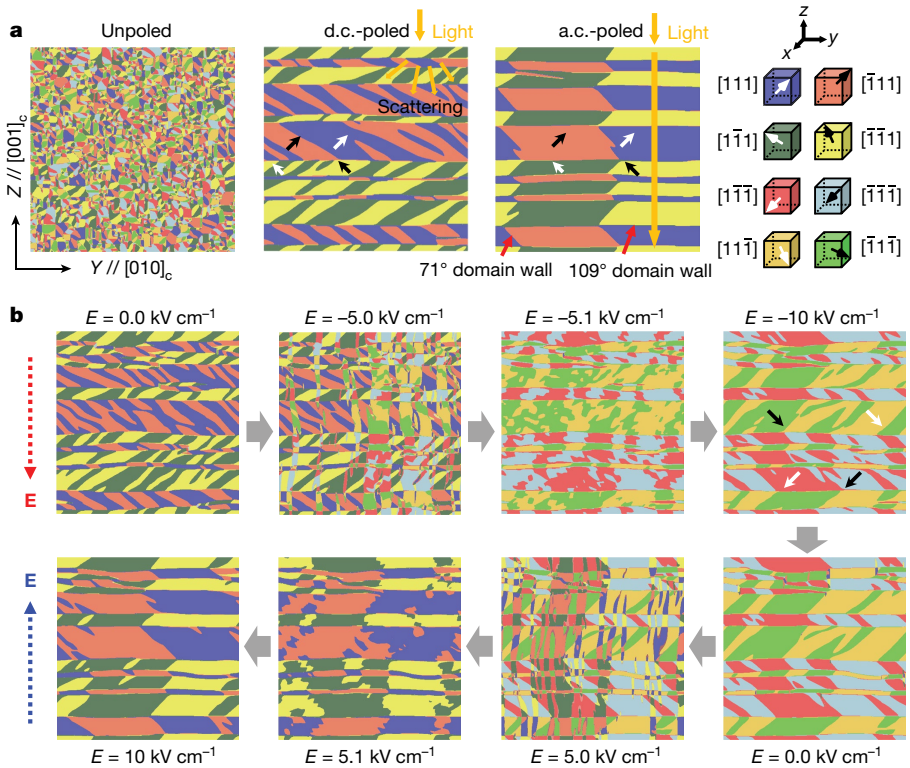

Fig. 1 | Phase-field simulations of the domain structures and evolution of [001]-oriented rhombohedral PMN-28PT single crystals via d.c. and a.c. poling. a, Domain structures for unpoled, d.c.- and a.c.-poled samples. The subscript c denotes pseudo-cubic coordinates. The black and white vectors on the right show the polarization directions, and the colour denotes the positive (white) and negative (black) polarization components along the [100] direction. The other colours represent different ferroelectric domains (the corresponding polar directions are illustrated on the right). Examples of 71° and 109° domain walls are indicated by the red arrows. A beam of light is schematically illustrated in the d.c.- and a.c.-poled cases, indicating that the light may not be scattered as it travels through the a.c.-poled sample. **b**, Snapshots of the domain pattern evolution during the reversal of polarization under a.c. poling. The initial state (that is, electric field $E = 0.0\ \mathrm{kV\ cm^{-1}}$) is the d.c.-poled sample. The blue and red arrows represent the applied electric fields along the [001] and [00$\bar{1}$] directions, respectively. The dimensions of all of the domain structure plots are 512 nm × 512 nm. The domain evolution under an a.c. electric field is shown in Supplementary Videos 1, 2. For comparison, the domain evolution under a d.c. electric field is shown in Supplementary Video 3.

In this work, we show that a.c. electric fields can be used to effectively eliminate light-scattering 71° domain walls for [001]-oriented rhombohedral PMN-PT crystals to achieve both near-perfect transparency and ultrahigh piezoelectricity. We first perform phase-field simulations to study the domain evolution of a [001]-oriented 0.72Pb($Mg_{1/3}Nb_{2/3}$)O_3-0.28$PbTiO_3$ (PMN-28PT) rhombohedral crystal using conventional d.c. and a.c. electric fields. We generate the initial pristine unpoled state starting from a random distribution of small polarizations that represent a high-temperature paraelectric state. The obtained multi-domain state contains all eight possible ⟨111⟩ rhombohedral domain variants with an average size of ~20 nm. Three types of domain wall are present in the unpoled rhombohedral crystal: 71°, 109° and 180° domain walls.

Under a d.c. electric field along the [001] direction, the four domain variants with polarizations along [11$\bar{1}$], [$\bar{1}$1$\bar{1}$], [$\bar{1}\bar{1}\bar{1}$] or [1$\bar{1}\bar{1}$] are switched to the [111], [1$\bar{1}$1], [$\bar{1}\bar{1}$1] or [$\bar{1}$11] directions. Thus, only 71° and 109° domain walls survive, whereas the 180° domain walls are eliminated, as shown Fig. 1a. The horizontal layers are separated by a set of 109° domain walls parallel to the (001) plane, whereas within each lamina there are 71° domain walls approximately parallel to {011} planes. It should be noted that 71° domain walls can scatter light because the refractive indices n_o and n_e (where o and e represent ordinary and extraordinary light, respectively) change as light travels across a 71° domain wall, as shown in Extended Data Fig. 1. By contrast, 109° domain walls do not induce light scattering as the refractive indices are the same for the domains on both sides of the wall.

Our phase-field simulations demonstrate that the application of an a.c. electric field effectively reduces the number of 71° domain walls, with only two 71° domain walls left in each lamina after a.c. poling, leading to a much larger domain size within each lamina. To understand the reason for the elimination of 71° domain walls by a.c. poling, we analyse the domain evolution during the polarization reversal process, as shown in Fig. 1b and Supplementary Videos 1, 2. One can see that the reversal of the electric field causes 'swinging' of 71° domain walls: that is, 71° domain walls alternate between the (011) and (01$\bar{1}$) planes. During this process, the contiguous 71° domains tend to merge with each other, resulting in a considerable increase in 71° domain size after a.c. poling. In addition (Extended Data Fig. 2), the total free energy of the system is reduced during this poling process as the energies arising from the discontinuities of polarization/strain associated with domain walls decrease when the domain wall density decreases. In other words, alternating the polarity of the electric field lowers the free energy of a ferroelectric crystal, leading to a domain structure with reduced domain wall density. As discussed above, owing to the substantially decreased 71° domain wall density, the light transmission of the a.c.-poled sample is expected to be superior to that of a corresponding d.c.-poled sample.

Following the phase-field simulations, we characterized the domain structures of a.c.-poled and d.c.-poled PMN-28PT crystals. Using birefringence imaging microscopy (BIM)[17], we characterized the orientation (φ) of the principal axis of the optical indicatrix projected on the (001) planes, as shown in Fig. 2a. For a rhombohedral single domain,

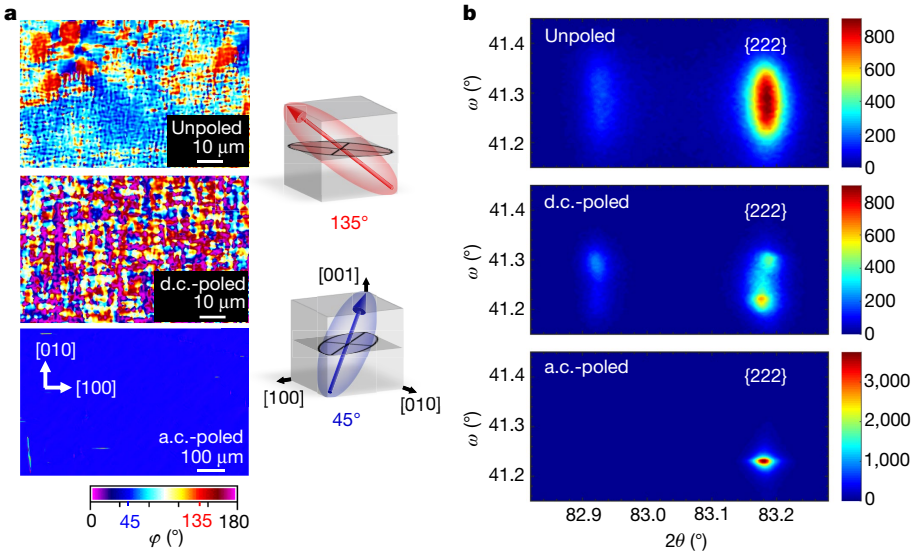

Fig. 2 | Analysis of the domain structures for the [001]-oriented PMN-28PT crystals. a, BIM image; the colours indicate the orientation angles (φ) of the projection of the principal optical axis on the (001) plane. Red and blue represent the projection of the principal axis of the optical indicatrix along the diagonal faces on the (001) plane, that is, φ of 45° and 135°, respectively. As an example, the projections of the principal axis of the optical indicatrix of the $[\bar{1}\bar{1}1]$ and $[1\bar{1}1]$ domains are illustrated in the schematics on the right of the figure. **b**, Reciprocal space maps of the {222} reflections from the samples under different poling conditions, measured with high-resolution single-crystal X-ray diffraction. The colour bars indicate the intensity of the diffraction. The thickness of the samples is 175 μm.

the projection of the optical axis is along the diagonal face. Therefore, the φ value of a rhombohedral domain would be 45° or 135°, which are represented by blue and red colours, respectively (colour bar in Fig. 2a). A multidomain crystal may show two or more colours simultaneously in the projection map owing to the overlap of ferroelectric domains and domain walls along the light propagation path.

The orientation map for the unpoled sample shows an irregular colour distribution on a very fine scale. This is because the domain size of the as-grown PMN-PT is much smaller than the experimental resolution (the wavelength of the light is 590 nm); therefore, the exact domain pattern may not be clearly revealed. Compared with classical ferroelectrics (for example, $BaTiO_3$), the relatively small domain size in relaxor ferroelectrics (of the order of several tens of nanometres before poling[18–20]) is attributed to the presence of random fields/bonds that inhibit the growth of ferroelectric domains[21–24].

After d.c. poling, the domains represented by regions with the same colour increase in size, and the boundaries between the domains are approximately along the [100] and [010] directions, which are associated with the projections of 71° domain walls ((101), $(10\bar{1})$, (011) or $(01\bar{1})$ planes) on the (001) plane. In this image, the colours of most regions are neither red nor blue. Of particular importance is the substantially enlarged domain size in the a.c.-poled sample, where the in-plane size of the rhombohedral domain is on the millimetre scale. It should be noted that the domain size obtained from the phase-field simulation is much smaller than that from experiments. This is because the spatial scale in the phase-field simulation (512 nm) is much smaller than that of the materials in the experiments (at the millimetre scale). By coarsening the scale in the phase-field simulation, the domain size of the a.c.-poled crystal is found to increase (Extended Data Fig. 3). It is difficult to perform a phase-field simulation on the millimetre scale and simultaneously resolve the polarization profiles across domain walls of ~1 nm in thickness. In this work, we used phase-field simulations to qualitatively analyse the domain evolution of PMN-28PT crystals during a.c. poling. We also characterized the cross-section domain structure of a.c.-poled and d.c.-poled samples to investigate the domain size in the out-of-plane direction. As shown in Extended Data Fig. 4, we found that the width between two neighbouring 109° domain walls is similar for both samples (~1 μm), indicating that most 109° domain walls survived after a.c. poling, which is consistent with the phase-field simulations.

X-ray diffraction patterns confirm the main observations from the BIM images. Figure 2b shows the {222} reflections for the [001]-oriented PMN-28PT crystals. If the rhombohedral domain variants are evenly distributed in the sample, there should be two diffraction peaks in the 2θ–ω map (2θ is the angle between the transmitted and reflected X-ray beams; ω represents the angle between the incident beam and the sample surface): one peak is associated with the (222) plane at a lower 2θ, and the other peak is associated with the remaining three {222} planes at a higher 2θ. Thus, the integrated intensity of the high-2θ reflection is supposed to be three times that of the low-2θ reflection. This is approximately what is observed in the unpoled sample. The diffused distribution of the diffraction along the ω axis is associated with the lattice distortions due to the existence of domain walls. The diffraction peaks converge into distinctive sharper reflections after d.c. poling, indicating that the domains become larger and that the volume fraction of domain walls decreases. Eventually, in the a.c.-poled sample, only the high-2θ diffraction peak is observed, and the diffusiveness of the diffraction peak along the ω axis is much smaller than that of the d.c.-poled and unpoled samples (Extended Data Fig. 5). These features reveal that the X-ray beam is approximately incident on a single domain of the a.c.-poled sample. The size of the beam here is about 1 mm^2, which indicates that the in-plane domain size of the a.c.-poled sample is equal to or larger than 1 mm^2.

Owing to the unique domain structure, a.c.-poled PMN-28PT crystals exhibit numerous attractive properties in addition to their ultrahigh piezoelectricity, including an electro-optical coefficient γ_{33} of 220 pm V^{-1}, near-perfect light transmittance and enhanced birefringence (Extended Data Table 1). Figure 3a shows photographs of the a.c.- and d.c.-poled samples: the a.c.-poled samples are clearly transparent. The light transmittance of the a.c.-poled sample is found to be very close to its theoretical limit and is much higher than that of the d.c.-poled sample, especially for the visible-light spectrum (Fig. 3b). The light with wavelengths below 400 nm is completely absorbed because of the optical absorption edge (~3.10 eV), which is similar to most oxygen

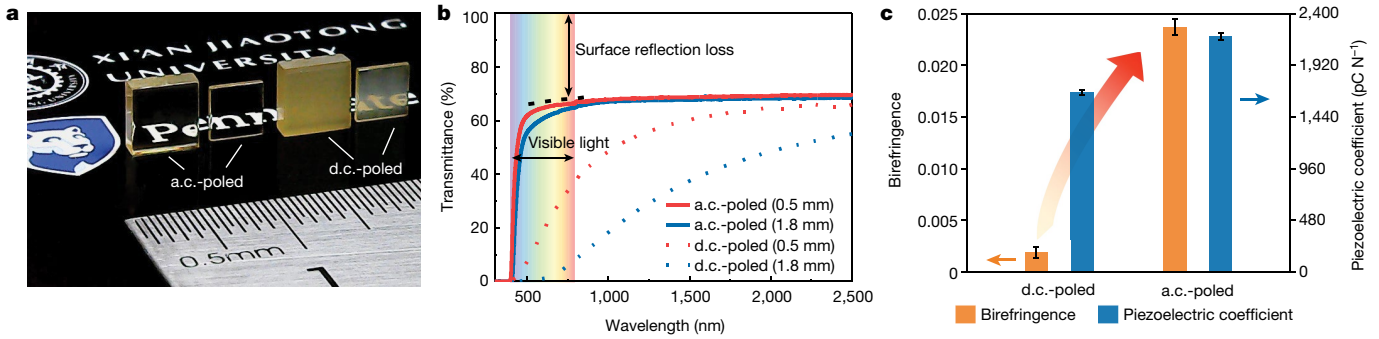

Fig. 3 | Comparison of the properties of a.c.-poled and conventional d.c.-poled [001]-oriented PMN-28PT crystals. a, Photograph of a.c- and d.c.-poled PMN-28PT crystals. The thicknesses of the crystals are 0.5 mm and 1.8 mm, respectively. **b**, Light transmittance of the a.c.- and d.c.-poled PMN-28PT crystals. **c**, d_{33} and birefringence of the a.c.- and d.c.-poled PMN-28PT crystals. Ten a.c.-poled and ten d.c.-poled samples are used for the characterization of d_{33}, whereas the birefringence is determined from seven points of the a.c.- and d.c.-poled samples. The red graded arrow indicates the increase in d_{33} and birefringence for PMN-PT crystals after a.c. poling. The error bars in **c** present the standard deviation of the corresponding data.

octahedral perovskites[25,26]. The light absorption coefficient of the a.c.-poled sample is found to be almost zero at wavelengths longer than 400 nm, whereas the absorption coefficient of the d.c.-poled sample remains large and decreases monotonically with increasing wavelength (Extended Data Fig. 6).

The birefringence of the a.c.-poled crystals is approximately one order of magnitude higher than that of their d.c.-poled counterparts (Fig. 3c). This difference is associated with the different domain structures. The principle axis of the optical indicatrices of the domains on both sides of a 71° domain wall are perpendicular to each other on the (001) plane, resulting in cancellation of the birefringence as light travels through a 71° domain wall (see Methods section 'PLM'). For a.c.-poled crystals, however, the birefringence is approximately equal to that of the intrinsic value of a single-domain rhombohedral PMN-28PT crystal because of the substantially decreased number of 71° domain walls.

The a.c.-poled crystals also exhibit a 30% enhancement in d_{33} over the d.c.-poled crystals. This phenomenon was observed in many a.c.-poled relaxor–PT crystals[27–30]. To understand the mechanism for the enhanced piezoelectricity, we conducted phase-field simulations to calculate the piezoelectricity of PMN-28PT with different 71° domain sizes, as shown in Fig. 4a. The variation of polar vectors around a 71° domain wall is depicted in Fig. 4b. For an ideal rhombohedral domain, the polar vectors are along the ⟨111⟩ directions, and the angle between the polar vector and the [011] direction is 35.3°. However, the presence of 71° domain walls causes the polar vectors to rotate towards the [011] direction to minimize the polarization gradient and elastic energies associated with the polarization/strain discontinuities around the

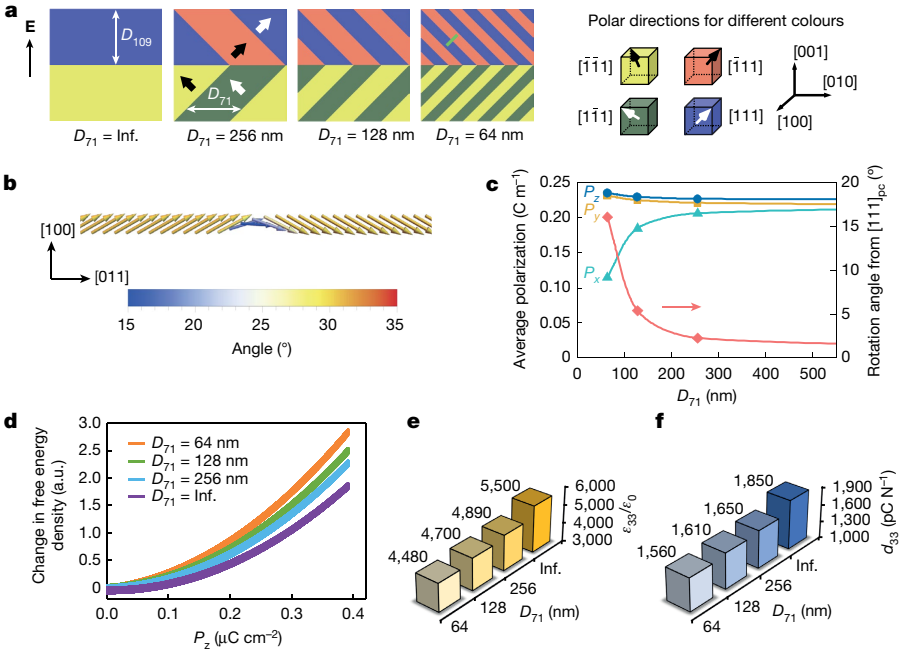

Fig. 4 | Phase-field simulations of the effect of domain size on the polarization, free-energy density and properties of the PMN-28PT crystal. a, Two-dimensional schematic of a [001]-poled PMN-28PT with various 71° domain widths (D_{71}). 'Inf.', no 71° domain walls are present in the system. The polar directions for different colours are depicted on the right. **b**, Schematic of polar vectors around a 71° domain wall (marked by the green line in **a**). The colours of the arrows represent the angles between each polar vector and the [011] direction. D_{71} in this schematic is 64 nm. **c**, The average magnitude of the spontaneous polarization components P_x ([100]), P_y ([010]) and P_z ([001]) of a ferroelectric domain as a function of D_{71}. The red line describes the angle between the overall polarization and the [111] direction as a function of D_{71}. **d**, The average free-energy density of the system with respect to P_z. The free-energy density at the stable state (that is, $\Delta P = 0$) is selected as the reference. **e**, Dielectric permittivity ($\varepsilon_{33}/\varepsilon_0$) as a function of D_{71}. **f**, d_{33} as a function of D_{71}.

domain walls. With decreasing domain size, the impact of the domain walls on the polarization becomes more prominent, resulting in a larger deviation of the polarization from the ⟨111⟩ directions, as shown in Fig. 4c. The free-energy profile of the system is also affected by the variation in polarization. As shown in Fig. 4d, the average free-energy profile of the system as a function of ΔP_z (the change in polarization P along the z direction; that is, the [001] direction) is flattened with the increase in the width of the 71° domains; that is, the curvature of the free-energy profile ($\partial^2 G/\partial P_z^2|_{\Delta P_z=0}$) decreases with increasing 71° domain width. Thus, the calculated ε_{33} and d_{33} increase with enlarging 71° domain widths, as shown in Fig. 4e, f.

It should be noted that the observed enhancement in piezoelectricity with increasing domain size is not universal to all ferroelectric crystals. It is expected that the piezoelectricity of ferroelectrics is also related to the symmetry of the ferroelectric phase and domain configurations[31,32]. For example, in tetragonal $BaTiO_3$ (refs. [8–10]) and high-temperature-poled PZN-PT crystals[33], where domain configurations are very different from PMN-28PT, the domain-size dependence of piezoelectricity shows an opposite trend to that observed here.

For the purpose of practical applications, we also studied the temperature stability of the properties of a.c.-poled PMN-28PT crystals (Extended Data Fig. 7), which indicates that the temperature-dependent electromechanical behaviours of a.c.- and d.c.-poled samples are very similar. Of particular interest is the fact that at temperatures below the rhombohedral–tetragonal phase transition temperature (~95 °C), the domain structure remains essentially the same, and no depolarization behaviour is observed, indicating that a.c.-poled crystals can be used up to their respective phase transition temperatures.

In summary, we report a simple approach that uses a.c. electric fields to simultaneously achieve near-perfect transparency, enhanced piezoelectricity and birefringence in rhombohedral PMN-PT crystals. Such transparent crystals are expected to find a wide range of applications in coupled electro-optical–mechanical devices. Both experimental and simulated results demonstrate that the enhanced piezoelectricity of [001]-oriented rhombohedral PMN-PT crystals achieved through a.c.-poling is due to the increased domain size, in contrast to the long-standing belief that decreasing domain size always leads to higher piezoelectricity.

Online content

Any methods, additional references, Nature Research reporting summaries, source data, extended data, supplementary information, acknowledgements, peer review information; details of author contributions and competing interests; and statements of data and code availability are available at https://doi.org/10.1038/s41586-019-1891-y.

1. Wang, L. V. Multiscale photoacoustic microscopy and computed tomography. *Nat. Photon.* **3**, 503–509 (2009).
2. Chen, X. et al. Transparent lead lanthanum zirconate titanate (PLZT) ceramic fibers for high-frequency ultrasonic transducer applications. *Ceram. Int.* **42**, 18554–18559 (2016).
3. Tshering, C. & Tshering, D. Renewable mobile charger using piezoelectric transducer. *Res. J. Recent Sci.* **7**, 20–23 (2018).
4. Sette, D. et al. Transparent piezoelectric transducers for large area ultrasonic actuators. In *2017 IEEE 30th International Conference on Micro Electro Mechanical Systems (MEMS)*. 793–796 (IEEE, 2017).
5. Modarres, A., Ramstein, C., Cruz-Hernandez, J. M., Danny, A. & Grant, A. G. Transparent composite piezoelectric combined touch sensor and haptic actuator. US Patent 2011/0261021 A1 (2011).
6. Thalhammer, G., McDougall, C., MacDonald, M. P. & Ritsch-Marte, M. Acoustic force mapping in a hybrid acoustic-optical micromanipulation device supporting high resolution optical imaging. *Lab Chip* **16**, 1523–1532 (2016).
7. Niederhauser, J. J., Jaeger, M., Hejazi, M., Keppner, H. & Frenz, M. Transparent ITO coasted PVDF transducer for optoacoustic depth profiling. *Opt. Commun.* **253**, 401–406 (2005).
8. Wada, S., Yako, K., Kakemoto, H., Tsurumi, T. & Kiguchi, T. Enhanced piezoelectric properties of barium titanate single crystals with different engineered-domain sizes. *J. Appl. Phys.* **98**, 014109 (2005).
9. Hlinka, J., Ondrejkovic, P. & Marton, P. The piezoelectric response of nanotwinned $BaTiO_3$. *Nanotechnology* **20**, 105709 (2009).
10. Ahluwalia, R., Lookman, T., Saxena, A. & Cao, W. Domain-size dependence of piezoelectric properties of ferroelectrics. *Phys. Rev. B* **72**, 014112 (2005).
11. Jaffe, B., Cook, W. R. & Jaffe, H. *Piezoelectric Ceramics* (Academic, 1971).
12. Damjanovic, D. Comments on origins of enhanced piezoelectric properties in ferroelectrics. *IEEE Trans. Ultrason. Ferroelectr. Freq. Control* **56**, 1574–1585 (2009).
13. Sun, E. W. & Cao, W. W. Relaxor-based ferroelectric single crystals: growth, domain engineering, characterization and applications. *Prog. Mater. Sci.* **65**, 124–210 (2014).
14. Zhang, S. J. et al. Advantages and challenges of relaxor-PT ferroelectric crystals for electroacoustic transducers—a review. *Prog. Mater. Sci.* **68**, 1–66 (2015).
15. Haertling, G. H. Ferroelectric ceramics: history and technology. *J. Am. Ceram. Soc.* **82**, 797–818 (1999).
16. Ruan, W. et al. Large electro-optic effect in La-doped $0.75Pb(Mg_{1/3}Nb_{2/3})O_3$-$0.25PbTiO_3$ transparent ceramic by two-stage sintering. *J. Am. Ceram. Soc.* **93**, 2128–2131 (2010).
17. Glazer, A. M., Lewis, J. G. & Kaminsky, W. An automatic optical imaging system for birefringent media. *Proc. R. Soc. Lond. A* **452**, 2751–2765 (1996).
18. Shvartsman, V. & Kholkin, A. Domain structure of $0.8Pb(Mg_{1/3}Nb_{2/3})O_3$-$0.2PbTiO_3$ studied by piezoresponse force microscopy. *Phys. Rev. B* **69**, 014102 (2004).
19. Bai, F., Li, J. & Viehland, D. Domain hierarchy in annealed (001)-oriented Pb $(Mg_{1/3}Nb_{2/3})O_3$-*x*% $PbTiO_3$ single crystals. *Appl. Phys. Lett.* **85**, 2313–2315 (2004).
20. Sato, Y., Hirayama, T. & Ikuhara, Y. Real-time direct observations of polarization reversal in a piezoelectric crystal: $Pb(Mg_{1/3}Nb_{2/3})O_3$-$PbTiO_3$ studied via in situ electrical biasing transmission electron microscopy. *Phys. Rev. Lett.* **107**, 187601 (2011).
21. Kleemann, W. Relaxor ferroelectrics: cluster glass ground state via random fields and random bonds. *Phys. Stat. Sol. B* **251**, 1993–2002 (2014).
22. Bokov, A. A. & Ye, Z. G. Recent progress in relaxor ferroelectrics with perovskite structure. *J. Mater. Sci.* **41**, 31–52 (2006).
23. Krogstad, M. J. et al. The relation of local order to material properties in relaxor ferroelectrics. *Nat. Mater.* **17**, 718–724 (2018).
24. Takenaka, H., Grinberg, I., Liu, S. & Rappe, A. M. Slush-like polar structures in single-crystal relaxors. *Nature* **546**, 391–395 (2017).
25. Wan, X. M., Luo, H. S., Wang, J., Chan, H. L. W. & Choy, C. L. Investigation on optical transmission spectra of $(1–x)Pb(Mg_{1/3}Nb_{2/3})O_3$-$xPbTiO_3$ single crystals. *Solid State Commun.* **129**, 401–405 (2004).
26. Wemple, S. Polarization fluctuations and the optical-absorption edge in $BaTiO_3$. *Phys. Rev. B* **2**, 2679–2689 (1970).
27. Ogawa, T., Matsushita, M. & Tachi, Y. Domain controlled piezoelectric single crystal and fabrication method therefor. US Patent 2003/0178914 A1 (2003).
28. Yamashita, Y., Yamamoto, N., Hosono, Y. & Itsumi, K. Piezoelectric transducer, ultrasonic probe, and piezoelectric transducer manufacturing method. US Patent 2015/0372219 A1 (2015).
29. Chang, W. Y. et al. Dielectric and piezoelectric properties of $0.7Pb(Mg_{1/3}Nb_{2/3})O_3$-$0.3PbTiO_3$ single crystal poled using alternating current. *Mater. Res. Lett.* **6**, 537–544 (2018).
30. Xu, J. et al. Piezoelectric performance enhancement of $Pb(Mg_{1/3}Nb_{2/3})O_3$-$0.25PbTiO_3$ crystals by alternating current polarization for ultrasonic transducer. *Appl. Phys. Lett.* **112**, 182901 (2018).
31. Budimir, M., Damjanovic, D. & Setter, N. Piezoelectric response and free-energy instability in the perovskite crystals $BaTiO_3$, $PbTiO_3$, and $Pb(Zr,Ti)O_3$. *Phys. Rev. B* **73**, 174106 (2006).
32. Sluka, T., Tagantsev, A. K., Damjanovic, D., Gureev, M. & Setter, N. Enhanced electromechanical response of ferroelectrics due to charged domain walls. *Nat. Commun.* **3**, 748 (2012).
33. Xiang, Y., Zhang, R. & Cao, W. Optimization of piezoelectric properties for $[001]_c$ poled 0.94 Pb $(Zn_{1/3}Nb_{2/3})O_3$–0.06 $PbTiO_3$ single crystals. *Appl. Phys. Lett.* **96**, 092902 (2010).

Methods

Sample preparation

To achieve high transparency in the rhombohedral PMN-PT crystals, we choose crystal compositions that avoid the presence of multiple phases, such as a mixture of rhombohedral, monoclinic and orthorhombic phases within an MPB region. In particular, we selected the 28% PT composition to circumvent the MPB region (around 33% PT). The PMN-28PT single crystals were grown by a modified Bridgman method at Xi'an Jiaotong University. The crystals were oriented by an X-ray diffraction (XRD) method with the x, y and z axes along the [100], [010] and [001] directions, respectively, and then cut to the required dimensions for different experiments. The thickness of the samples for the domain observations and birefringence measurements was 0.175 mm. For the other experiments, the thickness of the samples was in the range of 0.5 mm to 4 mm. Vacuum-sputtered gold was applied to both (001) faces of the samples to act as electrodes.

The a.c.- and d.c.-poling experiments were performed with a ferroelectric test system (TF Analyzer 2000E, aixACCT) with a high-voltage amplifier (TREK 610E). The samples were immersed in silicone oil during the poling process. For a.c. poling, a bipolar triangle wave was applied to the samples with a frequency of 0.1–100 Hz, a cycle number of 5–20, an amplitude of 5 kV cm^{-1} and a poling temperature of 20–60 °C (ref. [34]). We discovered that essentially all of the 71° domain walls could be effectively eliminated by using a.c. electric fields with a broad range of frequencies from 0.1 to 100 Hz (see Extended Data Fig. 8). The cycle number was selected to be larger than 10, as the enhancement of dielectric permittivity was found to saturate after 10 cycles, as shown in Extended Data Fig. 9. To minimize the fluctuations in dielectric and piezoelectric properties among different samples, the frequency of the a.c. electric field was selected to be below 10 Hz, as shown Extended Data Fig. 9. To minimize the influence of internal stresses generated during polishing and sputtering of PMN-28PT crystals, a thermal annealing process was applied to the PMN-28PT crystals before a.c. poling[34]. Specifically, the samples were first annealed at 300 °C for 5 h and then slowly cooled to room temperature. The samples then remained at room temperature for 5–7 days until the dielectric loss was reduced from approximately 4–5% after the annealing to around 2%. For the d.c. poling, a conventional poling process used for PMN-PT crystals was adopted, with a d.c. electric field amplitude of 5 kV cm^{-1} and a dwelling time of 5 min.

For the optical and XRD experiments, the gold electrodes were removed by a solution of potassium iodide and iodine (the mass ratio of KI:I_2:H_2O was 4:1:40) without affecting the polarization. The (001) surfaces were then carefully polished to optical quality using diamond polishing paste and decreasing the average grit size down to 0.05 μm. For the electro-optic measurements, a thin layer of gold film (~15 nm) was deposited on the polished surfaces to act as electrodes. Silver leads were attached using conductive epoxy to apply a voltage.

Here, we would like to note that there are two technical issues associated with the idea of using crystals poled along the [111] direction and then cut along the [001] direction to achieve both a high d_{33} and light transparency rather than the a.c. poling employed in this work.

(1) The limitations of crystal size and difficulty in achieving a single domain state by poling [111] oriented rhombohedral crystals. For example, if one needs a [001]-oriented crystal plate with a size of 20 mm × 20 mm × 1 mm (the practical size of piezoelectric materials for medical transducers is in the range of 20–60 mm), one first needs a [111]-oriented crystal with the size of ~30 × 30 × 30 mm^3. It is almost impossible to pole a crystal with a thickness of 30 mm along its spontaneous polarization direction as the internal stresses that develop during poling induce severe cracking[35]. In addition, one cannot guarantee a homogeneous composition for the [001]-oriented crystal plates made using this process because of the composition segregation along the growth direction of Bridgman-grown PMN-PT crystal boules.

(2) The instability of a single-domain state and the issue of depolarization. Preparing the [111]-poled samples with a rotated d_{33} involves high-temperature processes, such as attaching a crystal to a sample holder for cutting, heat generation during cutting and sputtering transparent electrodes (the temperature required for sputtering ITO electrodes is approximately 300–600 °C). One may argue that we can adopt careful, low-temperature processes and utilize low-temperature transparent electrodes (such as silver nanowires) to prepare the samples. However, based on our experience, this is a difficult task, as we need to use special binders and sample holders and drastically slow down the cutting speed of the cutting machine; the adhesion of electrodes would also be substantially affected by using silver nanowires in place of ITO. Even if all of these precautions and approaches are followed, the samples are still likely to be depolarized to some extent because of the instability of a single-domain state. In addition, the [001]-oriented samples made by this process cannot be re-poled if they are de-poled accidentally. This is due to the fact that we cannot recover the original [111]-oriented samples.

Dielectric and piezoelectric measurements

The d_{33} values were determined by a combination of a quasi-static d_{33} meter (ZJ-6A) and an electric-field-induced strain measurement. The electric-field-induced strain was measured by a ferroelectric test system (TF Analyzer 2000E, aixACCT) with a laser interferometer (SIOS SP-S 120E). The dielectric permittivity was measured using an LCR meter (E4980A, KEYSIGHT technologies). To study the temperature stability of the properties, the d_{33} and k_{33} values of PMN-PT crystals are determined by the resonance method according to IEEE standard.

Optical transmittance measurements

Transmission spectra were measured with an ultraviolet–visible–infrared spectrophotometer (JASCO V-570) at wavelengths ranging from 300 to 2,500 nm. The incident light was set to transmit through the crystal along the poling direction, which was perpendicular to the (001) surface.

According to the Fresnel equations, the reflection loss at two faces of the crystal plate was calculated from 450 to 850 nm through:

$$R = \frac{(n-1)^2}{n^2+1} \tag{1}$$

where n is the wavelength-dependent index of refraction, calculated from the Sellmeier equation for a PMN-28PT single crystal given in refs. [36,37].

The effective loss coefficient α_{eff}, a combination of the scattering coefficient κ and the absorption coefficient α ($\alpha_{\text{eff}} = \kappa + \alpha$), was calculated using the transmission data from samples of different thicknesses:

$$\alpha_{\text{eff}} = -\frac{\ln(T_2/T_1)}{t_2 - t_1} \tag{2}$$

where T_1 and T_2 are the transmittances of the two samples with thicknesses t_1 and t_2, respectively.

Optical domain characterizations

PLM. The domain patterns and their extinction behaviours were observed using a PLM with a 0°/90° crossed polarizer/analyser pair (OLYMPUS BX51). The optical retardation was measured using a thick Berek compensator (OLYMPUS U-CTB, ~0–10λ) and an interference filter (IF546; wavelength, λ = 546.1 nm). The birefringence was calculated as the ratio of the retardation to the sample thickness. In the following, we would like to explain the cancellation effect of birefringence as light travels across a 71° domain wall. For a single-domain rhombohedral ferroelectric, the parameters Δn_1 and Δn_2 are the birefractive indices of two different domains on both sides of a 71° domain wall.

Because the principal axes of the optical indicatrices of the domains on both sides of a 71° domain wall (for example, the domains with polar vectors along [111] and [1$\bar{1}$1] directions) are perpendicular to each other on the (001) plane, the relation between Δn_1 and Δn_2 is $\Delta n_1 = -\Delta n_2$. Thus as the light travels across a 71° domain wall, the measured birefringence can be expressed by the following equation:

$$\Delta n^* = \frac{\Delta L}{d} = \frac{\Delta n_1 d_1 + \Delta n_2 d_2}{d_1 + d_2} = \Delta n_1 \frac{d_1 - d_2}{d} \quad (3)$$

where d_1 and d_2 are the lengths of optical path within the [111] and [1$\bar{1}$1] domains, respectively, ΔL is the optical retardation caused by birefringence, and d is a sum of d_1 and d_2. It is obvious that the measured birefringence will be quite small if the values of d_1 and d_2 are similar.

BIM. The domain orientation measurements were performed using BIM equipment (Metripol, Oxford Cryosystems). Monochromatic light with a wavelength of 590 nm was used as the light source. A quarter-wave plate and a polaroid (P_2) were placed at a 45° position to produce circularly polarized light. The circularly polarized light was converted to elliptical polarization after passing through an optically anisotropic specimen. The light then transmits through a linear analyser (P_2) rotating about the microscope axis at a frequency of ω. Finally, the intensity measured by the charge-coupled device (CCD) camera as a function of ω is given by

$$I = \frac{1}{2} I_0 \{1 + \sin[2(\omega t - \varphi)] \sin\delta\} \quad (4)$$

where t is the time, φ is the angle between the horizontal direction and the principal axis of the optical indicatrix, δ is the phase shift introduced to the light rays passing through the anisotropic sample with a certain thickness, and I_0 is the intensity of the unpolarized light. After rotating the analyser ten times, it is possible to obtain the intensity of each pixel on the recorded image, refine the I_0, $|\sin\delta|$ and φ values, and construct the false-colour images.

High-resolution XRD experiments

High-resolution, single-crystal XRD experiments were carried out to analyse the {222} Bragg reflections for (001)-oriented PMN-PT crystals. A high-resolution diffractometer (PANalytical X'Pert Pro MRD), equipped with Cu Kα_1 radiation, a hybrid mirror monochromator, an open Eulerian cradle and a solid-state PIXcel detector, was used for a precise two-dimensional 2θ–ω scan of the {222} Bragg peaks. The reciprocal space maps were collected with step sizes of 0.004° in ω and 0.004° in 2θ. The intensity of the patterns was accumulated along the ω or 2θ directions and then fitted to the pseudo-Voigt function:

$$f(x) = a_1 \left\{ a_4 \frac{1}{1 + \left(\frac{x - a_2}{a_3}\right)^2} + (1 - a_4) \exp\left[-\left(\frac{x - a_2}{a_3}\right)^2 \right] \right\} \quad (5)$$

where a_1 is the intensity of the peak, a_2 is the position of the peak, a_4 is the mixing parameter of the Gaussian and Lorentzian profiles, and a_3 is proportional to the full-width at half-maximum (FWHM), which can be calculated using the equation,

$$\mathrm{FWHM} = 2\sqrt{\ln 2}\, a_3 \quad (6)$$

Electro-optic measurements

The electro-optic coefficients of the samples were measured using a modified Mach–Zehnder interferometer. The light source was a 632.8-nm He–Ne laser. For the longitudinal mode, the light beam and the applied electric field were both parallel to the poling direction. In this mode, the longitudinal effective linear electro-optic coefficient γ_c^{L*} was measured, where the subscript c indicates that the coefficient is a composite of several electro-optic coefficients in the standard coordinate system (for example, r_{13} and r_{33}).

For the transverse mode, the light beam travels along the [110] direction, and the electric field was applied along the [001] poling direction of the sample. The linear electro-optic coefficients γ_{13}^* and γ_{33}^* were measured when the polarization directions of the laser beam were perpendicular and parallel to the poling direction, respectively. The transverse effective linear electro-optic coefficient (γ_c^{T*}) was calculated by the equation:

$$\gamma_c^{T*} = \gamma_{33}^* - n_0^3 \gamma_{13}^* / n_e^3 \quad (7)$$

The refractive indices were calculated from the data of single-domain crystals[36,37]. The asterisk indicates that the measured electro-optic coefficient is a combination of the inverse piezoelectric effect and the intrinsic electro-optic effect.

Phase-field simulations

The domain evolution and piezoelectric responses were obtained by performing phase-field simulations. A domain structure is described by the spatial distribution of the ferroelectric polarization **P**. The temporal evolution of the polarization and thus the domain structure is described by the time-dependent Ginzburgh–Landau equation:

$$\frac{\partial \mathbf{P}}{\partial t} = -L \frac{F(\mathbf{P})}{\delta \mathbf{P}} \quad (8)$$

where t is the time, F is the total free energy and L is the kinetic coefficient. The total free energy contains contributions from the bulk, elastic, electric and gradient energies. Details of how the phase-field method can be used to simulate the switching behaviours of ferroelectric single crystals can be found in refs. [38,39]. The Landau coefficients were adapted from ref. [40] using the experimental ferroelectric, piezoelectric and dielectric properties of PMN-28PT crystals at room temperature. On the basis of this thermodynamic potential, the calculated equilibrium phase is rhombohedral at room temperature with a spontaneous polarization of ~0.38 C m^{-2}, a relative dielectric constant of ~5,500 along [001] and a longitudinal piezoelectric coefficient of ~1,850 pC N^{-1} along [001], which are in reasonable agreement with our experiments. The electrostrictive coefficients measured by Li et al.[41] for PMN-28PT were adopted. The gradient energy coefficients were assumed to be isotropic, and the domain wall width was assumed to be ~2 nm. It should be noted here that the Landau potential used in this work represents the average free energy of a single-domain PMN-28PT crystal, which incorporates the impacts of the nanoscale heterogeneous polar regions (several nanometres) in the free energy and electromechanical properties[42].

To simulate the a.c. and d.c. poling processes, we first obtained an unpoled domain structure from a random noise distribution of the polarization within a quasi-two-dimensional grid with $512\Delta x \times 512\Delta x \times 1\Delta x$ grid points ($\Delta x = 1$ nm). A low-frequency triangle wave was then applied to mimic the a.c. poling, whereas a single-step square wave was used to represent the d.c. poling. The magnitude of the poling electric field was 10 kV cm^{-1}. We performed phase-field simulations at different mechanical boundary conditions: the stress-free condition, which assumes the averaged stress of the simulated system is zero; and the clamped condition, which assumes the averaged strain is zero. Figure 1 shows the simulated results for the clamped condition, and the simulation results under stress-free conditions are presented in Extended Data Fig. 3b. The practical condition in the experiments is probably between these two extreme mechanical conditions. The conclusion that the sizes of the 71° domains in a.c.-poled samples are always much larger than the d.c.-poled ones holds for both mechanical boundary conditions, while the 109° domain layer thickness is similar

in both a.c.- and d.c.-poled samples. It is interesting to note that the a.c. poling can lead to a completely layered 109° domain structure without 71° domain walls under the stress-free condition.

The ε_{33} and d_{33} values were obtained by evaluating the variations of polarization and longitudinal strain under a small electric field of 0.5 kV cm^{-1} along the [001] direction. We also calculate the free energy by applying small test electric fields (E_z is from 0 to 1 kV cm^{-1}, which is sufficiently small to avoid domain wall motion or phase transitions) and plot the average free-energy density as a function of the change of P_z along the poling direction.

The computer simulations were performed using the commercial software package μ-PRO (http://mupro.co/contact/) on the ICS-ACI Computing Systems at Pennsylvania State University and at the Extreme Science and Engineering Discovery Environment cluster, which used the Bridges system at the Pittsburgh Supercomputing Center[43,44].

Data availability

The data that support the findings of this study are available on request from the corresponding authors.

34. Li, F. et al. Transparent ferroelectric crystals with ultrahigh piezoelectricity. Provisional US Patent 16/541,309 (2019).
35. Li, F., Wang, L., Jin, L., Xu, Z. & Zhang, S. J. Achieving single domain relaxor-PT crystals by high temperature poling. *CrystEngComm* **16**, 2892–2897 (2014).
36. Wan, X. M., Chan, H. L. W., Choy, C. L., Zhao, X. & Luo, H. Optical properties of (1–x) $Pb(Mg_{1/3}N_{b2/3})O_3$-x$PbTiO_3$ single crystals studied by spectroscopic ellipsometry. *J. Appl. Phys*. **96**, 1387–1391 (2004).
37. Wan, X. M. et al. Refractive indices and linear electro-optic properties of (1–*x*) $Pb(Mg_{1/3}N_{b2/3})O_3$-*x*$PbTiO_3$ single crystals. *Appl. Phys. Lett*. **85**, 5233–5235 (2004).
38. Wang, J., Shi, S. Q., Chen, L.-Q., Li, Y. & Zhang, T. Y. Phase-field simulations of ferroelectric/ferroelastic polarization switching. *Acta Mater*. **52**, 749–764 (2004).
39. Wang, J., Wang, B. & Chen, L.-Q., Understanding, predicting, and designing ferroelectric domain structures and switching guided by the phase-field method. *Annu. Rev. Mater. Res*. **49**, 127–152 (2019).
40. Khakpash, N., Khassaf, H., Rossetti, G. A. Jr & Alpay, S. P. Misfit strain phase diagrams of epitaxial PMN-PT films. *Appl. Phys. Lett*. **106**, 082905 (2015).
41. Li, F., Jin, L., Xu, Z., Wang, D. & Zhang, S. J. Electrostrictive effect in $Pb(Mg_{1/3}Nb_{2/3})O_3$-*x* $PbTiO_3$ crystals. *Appl. Phys. Lett*. **102**, 152910 (2013).
42. Li, F. et al. The origin of ultrahigh piezoelectricity in relaxor-ferroelectric solid solution crystals. *Nat. Commun*. **7**, 13807 (2016).
43. Towns, J. et al. XSEDE: accelerating scientific discovery. *Comput. Sci. Eng*. **16**, 62–74 (2014).
44. Nystrom, N. A., Levine, M. J., Roskies, R. Z. & Scott, J. R. Bridges: a uniquely flexible HPC resource for new communities and data analytics. In *Proc. 2015 Annual Conference on Extreme Science and Engineering Discovery Environment* (ACM, 2015); https://doi.org/10.1145/2792745.2792775.

Acknowledgements F.L. and Z.X. acknowledge the support of the National Natural Science Foundation of China (grant numbers 51922083, 51831010 and 51761145024), the development programme of Shaanxi province (grant number 2019ZDLGY04-09) and the 111 Project (B14040). B.W. and L.Q.C. acknowledge the support of the US National Science Foundation under the grant number DMR-1744213 and Materials Research Science and Engineering Center (MRSEC) grant number DMR-1420620. N.Z. thanks the NSFC for support under grant number 1604123. The computer simulations were performed on the ICS-ACI Computing Systems at Pennsylvania State University through the Penn State Institute for Cyber Science and at the Extreme Science and Engineering Discovery Environment cluster supported by National Science Foundation grant number ACI-1548562; the Bridges system was used, which is supported by NSF award number ACI-1445606 at the Pittsburgh Supercomputing Centre under the allocation DMR170006. S.Z. thanks the ONRG (grant number N62909-18-12168) and ARC (grant number FT140100698) for support. T.R.S. was supported by the US ONR.

Author contributions The work was conceived and designed by S.Z., L.Q.C. and F.L. C.Q. performed the piezoelectric and optical experiments. F.L. and Z.X. supervised the piezoelectric and dielectric measurements. N.Z. and F.L. supervised the optical experiments. B.W. performed the phase-field simulations and discussed with F.L. L.Q.C. supervised the simulation work. J.L. assisted with the piezoelectric measurements. N.Z. and D.W. performed XRD experiments. Y.W. and H.T. assisted with the optical measurements. F.L. drafted the manuscript, S.Z., N.Z., L.Q.C. and T.R.S. revised the manuscript and all authors discussed the results.

Competing interests The authors declare no competing interests.

Additional information

Supplementary information is available for this paper at https://doi.org/10.1038/s41586-019-1891-y.

Correspondence and requests for materials should be addressed to Z.X., L.-Q.C. or F.L.

Peer review information *Nature* thanks Wook Jo and the other, anonymous, reviewer(s) for their contribution to the peer review of this work.

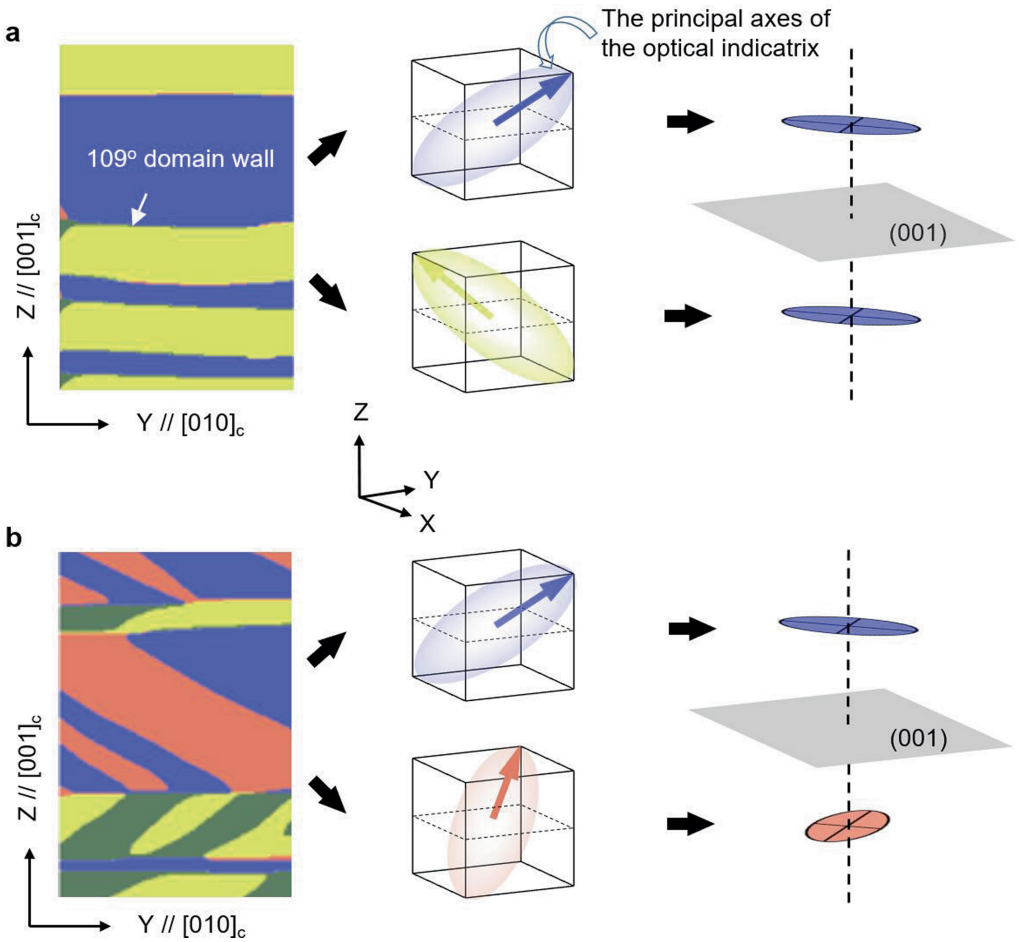

Extended Data Fig. 1 | Schematic diagrams of the projections of optical indicatrices on both sides of a domain wall. a, 109° domain wall; **b**, 71° domain wall. The prerequisite for the light scattering and reflection at an interface is the difference in refractive indices between the optical media on each side of the interface. As shown here, the principal axes of the optical indicatrix projected on the (001) plane are the same for domains on each side of a 109° domain wall. Thus, n_o and n_e do not change as the light crosses a 109° domain wall, resulting in the absence of light scattering and/or reflection. In contrast, the principal axis of the optical indicatrix projected on the (001) plane rotates by 90° as the light travels across a 71° domain wall, resulting in the alternating of refractive indices n_o and n_e. This is the reason that 71° domain walls scatter and/or reflect the light.

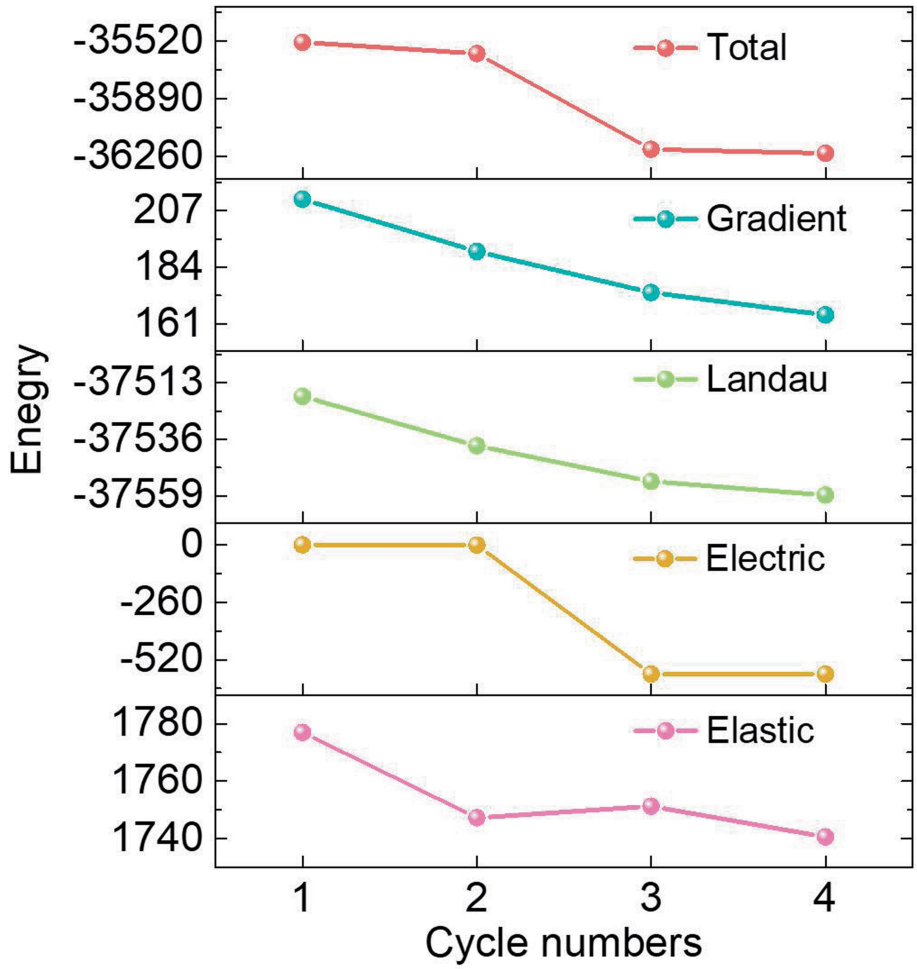

Extended Data Fig. 2 | The variation in various energies of PMN-28PT during the first four cycles of a.c. poling. The data are obtained by phase-field simulations. Here we plot the normalized energies, which are dimensionless.

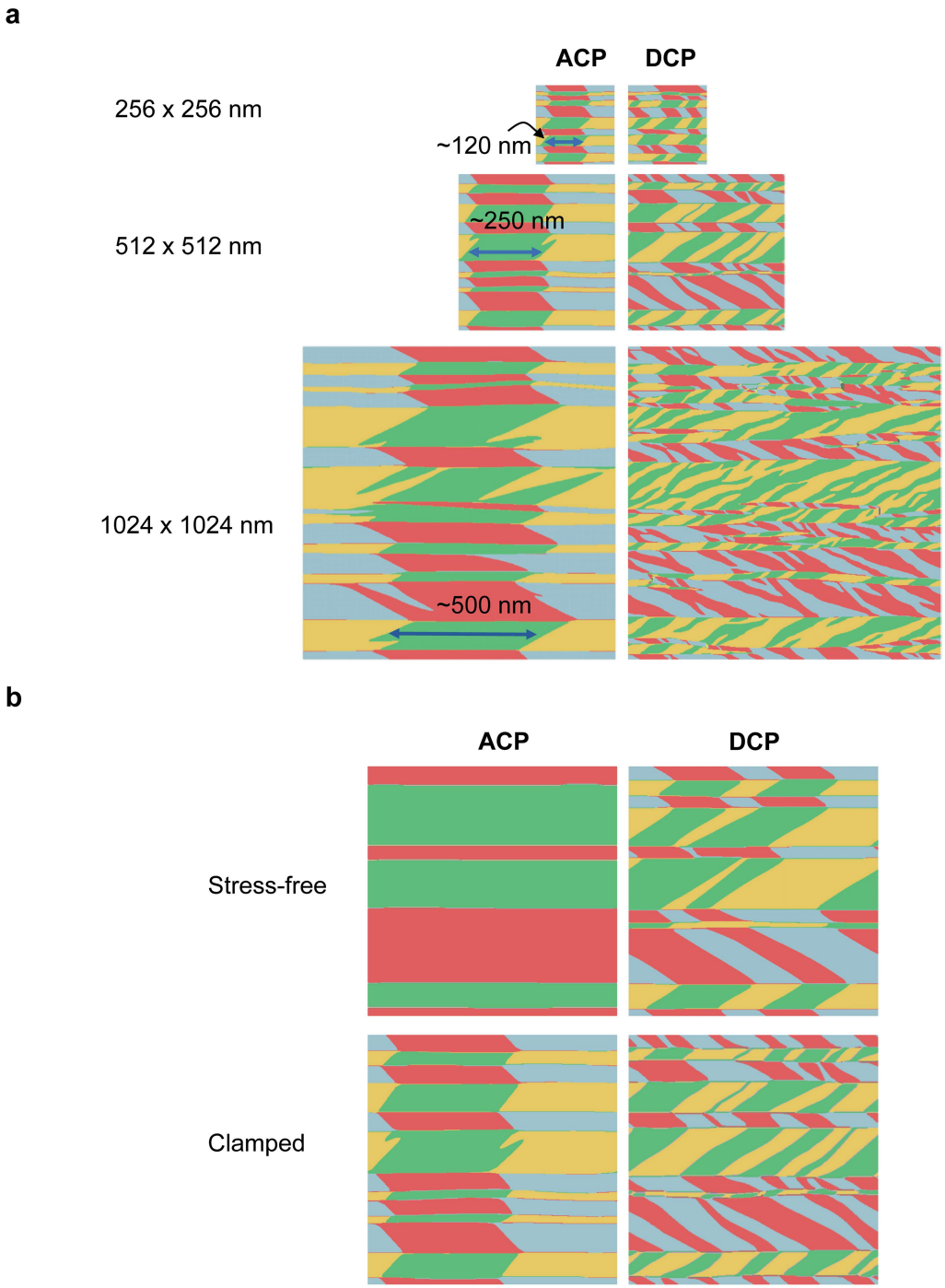

Extended Data Fig. 3 | Effects of system size and mechanical boundary conditions on the a.c.- and d.c.-poled domain structures from phase-field simulations. **a**, Effects of system size (at the clamped boundary condition). **b**, Effects of the mechanical boundary condition (the scale of the simulation is 512 × 512 nm).

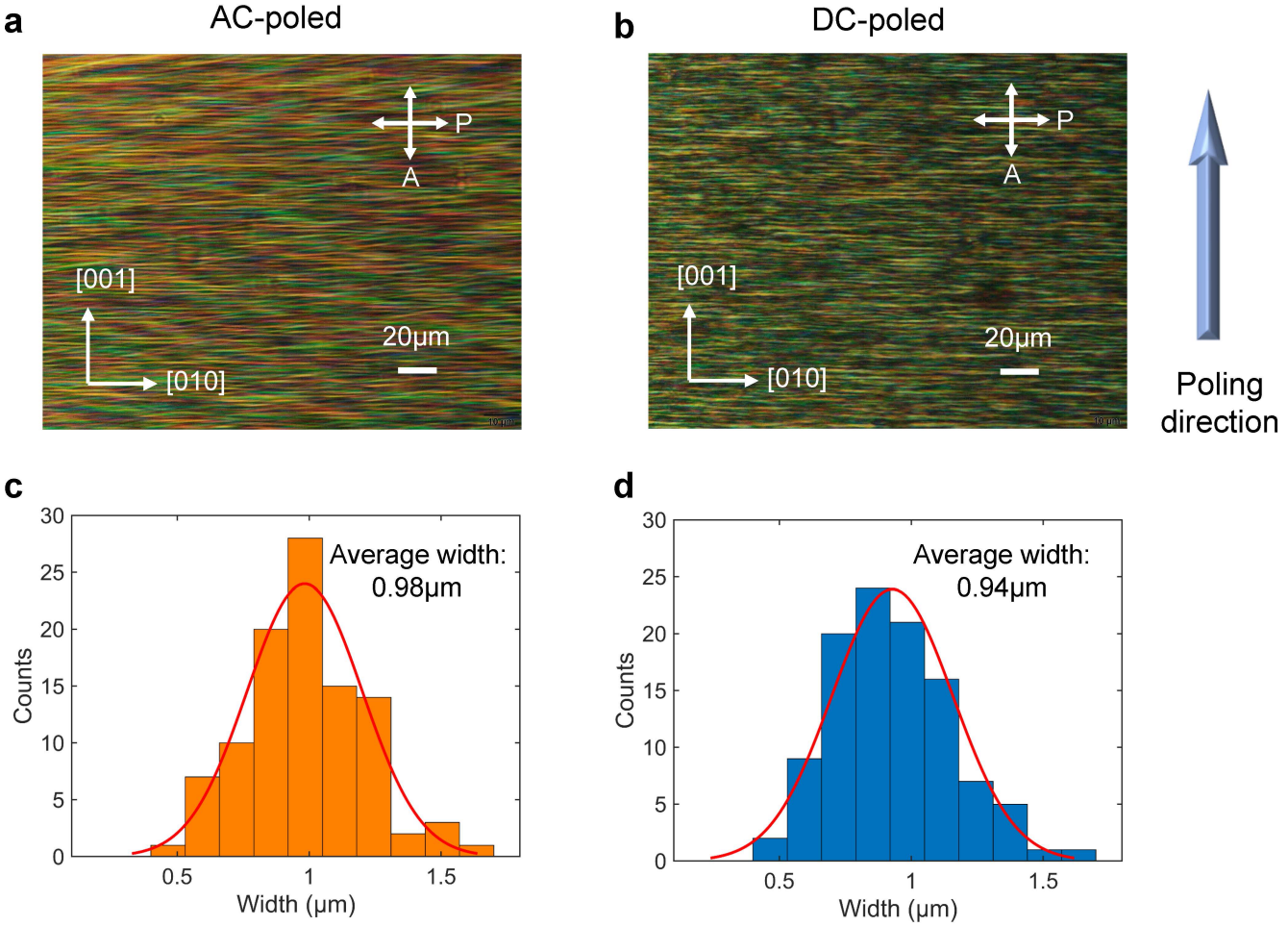

Extended Data Fig. 4 | Characterization of the domain size along the poling direction for [001]-oriented rhombohedral PMN–PT crystals. a, PLM images on the (100) face for [001]-poled PMN-28PT crystals under a.c. poling. **b**, PLM images on the (100) face for [001]-poled PMN-28PT crystals under d.c. poling. **c**, Distribution of the thickness of laminar domains for the a.c.-poled sample measured from **a**. **d**, Distribution of the thickness of laminar domains for the d.c.-poled sample measured from **b**. The thickness of the samples is around 100 μm. As shown in this figure, no clear difference is observed for the thickness of laminar domains between a.c.- and d.c.-poled samples.

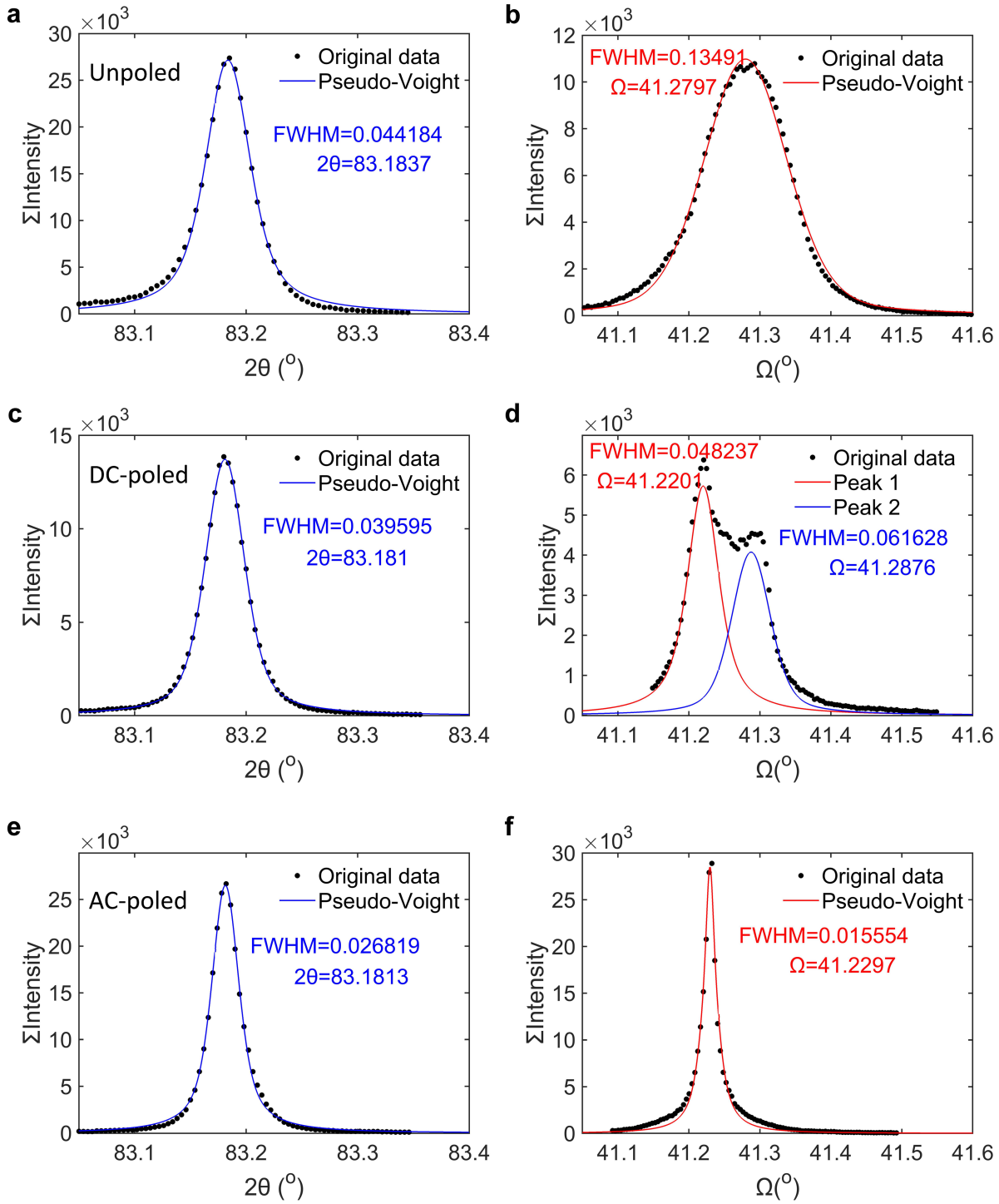

Extended Data Fig. 5 | Pseudo-Voight fittings of the {222} diffraction peaks at high-2θ. a,**b**, The unpoled sample. **c**,**d**, The d.c.-poled sample. **e**,**f**, The a.c.-poled sample. **a**,**c**,**e**, The intensity of the patterns accumulated along *Ω*. **b**,**d**,**f**, The intensity of the patterns accumulated along 2*θ*.

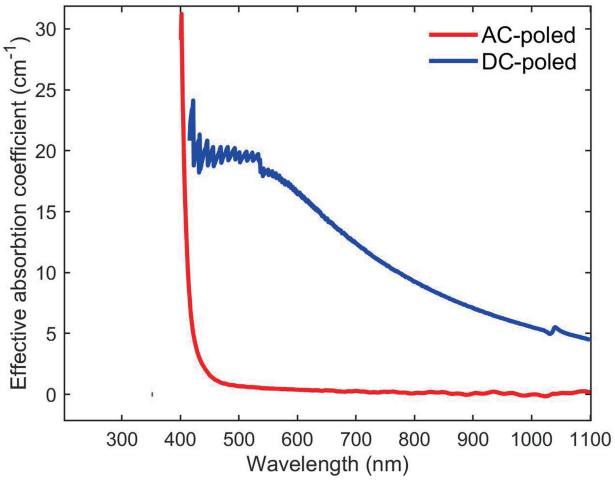

Extended Data Fig. 6 | Effective light absorption coefficients of a.c.- and d.c.-poled PMN-28PT crystals.

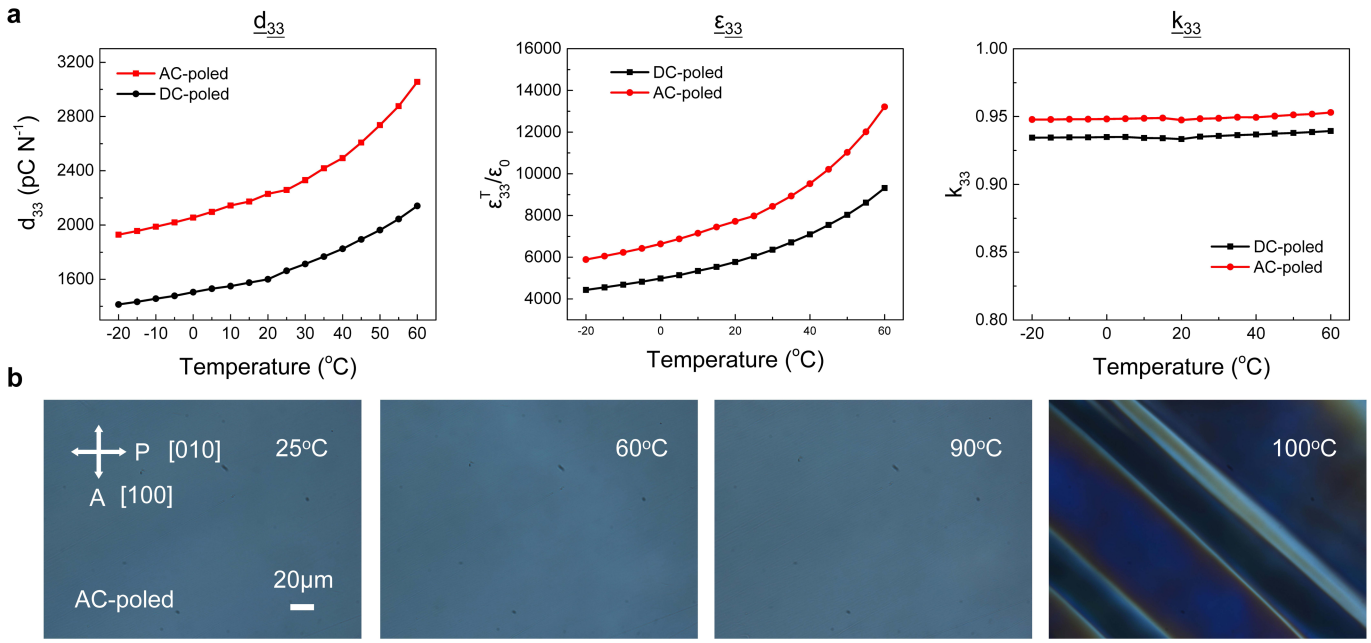

Extended Data Fig. 7 | The temperature stability of a.c.- and d.c.-poled PMN-28PT crystals. a, d_{33}, $\varepsilon_{33}^{T}/\varepsilon_0$ and k_{33} as a function of temperature. The dwelling time for each testing temperature is 10 min. **b**, Domain structure of a.c.-poled PMN-28PT crystals as a function of temperature. The temperature is increased from 25 to 100 °C at a rate of 1 °C min^{-1}. The dwelling time for each testing temperature is 30 min.

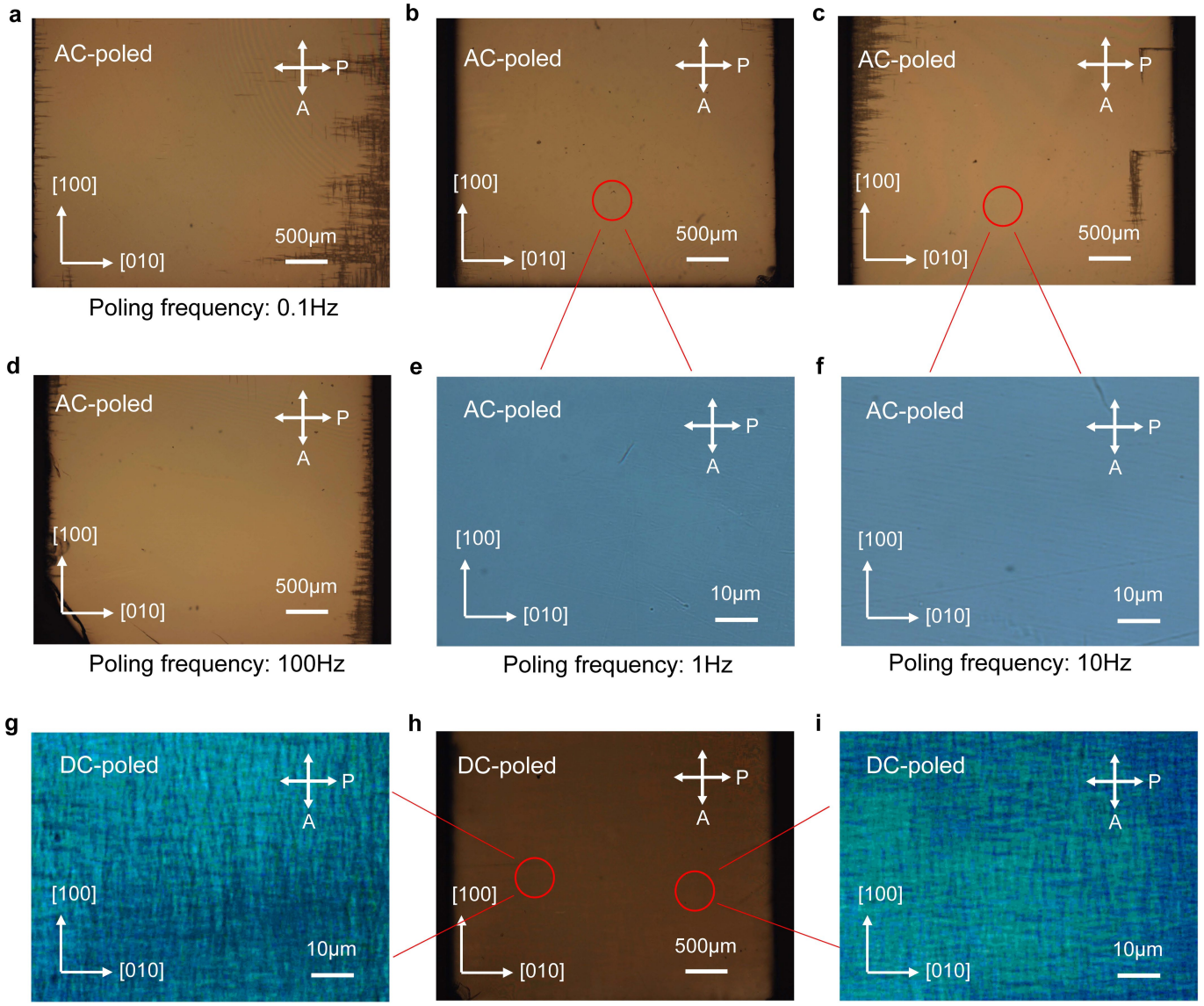

Extended Data Fig. 8 | PLM images of [001]-oriented PMN-28PT crystals with different poling conditions. a–**d**, Images obtained from the crystals poled by an a.c. electric field at frequencies of 0.1 Hz (**a**), 1 Hz (**b**), 10 Hz (**c**) and 100 Hz (**d**), respectively. **e**, **f**, Enlargements of the regions in **b** and **c**, respectively. **g**–**i**, Images obtained from the crystals poled by a d.c. electric field. **g**, **i**, Magnifications of the two regions circled in **h**. The thickness of the samples is 0.5 mm. There are numerous cross-like domain walls in d.c.-poled samples, whereas these types of domain wall are removed by an a.c. electric field.

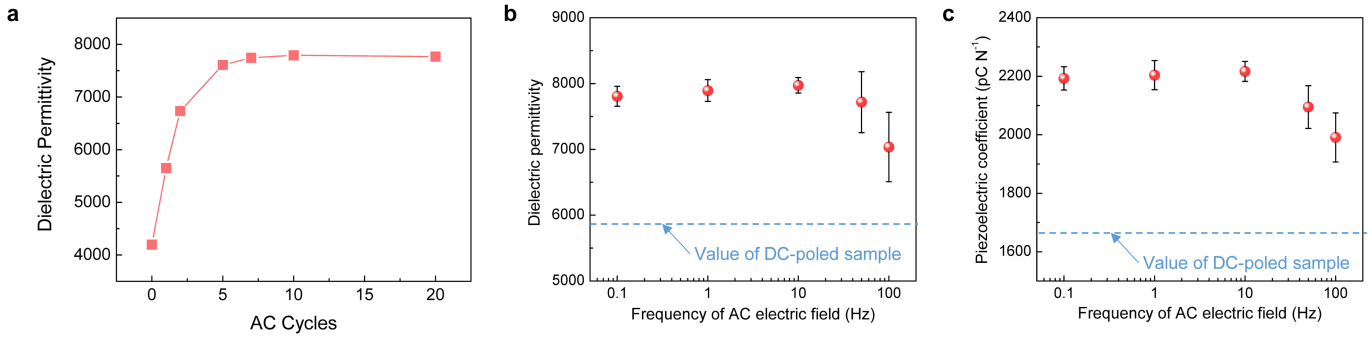

Extended Data Fig. 9 | Dielectric permittivity and piezoelectric coefficient of the a.c.-poled PMN-28PT crystal as a function of the cycle number and frequency. a, Dielectric permittivity as a function of the cycle number. **b**, Dielectric permittivity as a function of the frequency. **c**, Piezoelectric coefficient as a function of the frequency. Five samples are used for each frequency. The error bars indicate the s.d. of the corresponding data.

Extended Data Table 1 | Electromechanical and electro-optical properties of [001]-oriented PMN-28PT crystals via a.c.- and d.c.-poling

Properties of PMN-28PT	*DC*-poled	*AC*-poled
Free dielectric permittivity ($\varepsilon_{33}^{T}/\varepsilon_0$)	5800±120	7800±230
Clamped dielectric permittivity	780±50	840±60
Dielectric loss at 1 kHz (%)	0.48±0.02	0.30±0.04
Piezoelectric coefficient (pC N^{-1})	1670±30	2190±40
Electromechanical coupling factor k_{33}	0.93±0.01	0.94±0.01
Phase transition temperature T_{RT} (°C)	93±1	93±1
Curie temperature T_C (°C)	132±2	132±2
Birefringence (10^{-3})	1.89±0.55	23.7±0.7
Effective electro-optical coefficient γ_{33}^{*} (pm V^{-1}) @633nm light beam//[110]	-	227±23
Effective electro-optical coefficient γ_{13}^{*} (pm V^{-1}) @633nm light beam//[110]	-	115±11
Effective electro-optical coefficient γ_c^{L*} (pm V^{-1}) @633nm light beam//[001]	-	153±20

To measure γ_c^{L*}, both the applied electric field and the light beam are along the [001] direction. To measure coefficients γ_{33}^{*} and γ_{13}^{*}, the applied electric field is along the [001] direction, and the light beam is along the [110] direction. Note: it is difficult to obtain accurate electro-optical coefficients for d.c.-poled samples owing to the strong light scattering by the high density of ferroelectric domain walls. The errors indicate the s.d. of the corresponding data (more than five samples/data points are used for each measurement).